Title

Thalamic Roles in Conscious Perception Revealed by Low-Intensity Focused Ultrasound Neuromodulation

Author list

Hyunwoo Jang[1,2], Panagiotis Fotiadis[2,3], George A. Mashour[1,2,3,4,5], Anthony G. Hudetz[1,2,3,4], Zirui Huang[1,2,3,4,*]

Affiliations

[1] Neuroscience Graduate Program, University of Michigan, Ann Arbor, MI 48109, USA

[2] Center for Consciousness Science, University of Michigan Medical School, Ann Arbor, MI 48109, USA

[3] Department of Anesthesiology, University of Michigan Medical School, Ann Arbor, MI 48109, USA

[4] Michigan Psychedelic Center, University of Michigan Medical School, Ann Arbor, MI, 48109, USA

[5] Department of Pharmacology, University of Michigan Medical School, Ann Arbor, MI, 48109, USA

* Correspondence and requests for materials should be addressed to Z.H.

(Email: huangzu@med.umich.edu)

ABSTRACT

The neural basis of conscious perception remains incompletely understood. While cortical mechanisms of conscious content have been extensively investigated, the role of subcortical structures, including the thalamus, remains less explored. We aim to elucidate the causal contributions of different thalamic regions to conscious perception using transcranial low-intensity focused ultrasound (LIFU) neuromodulation. We hypothesize that modulating different thalamic regions would result in distinct perceptual outcomes. We apply LIFU in human volunteers to investigate region-specific and sonication parameter-dependent effects. We target anterior (transmodal-dominant) and posterior (unimodal-dominant) thalamic regions, further divided into ventral and dorsal regions, while participants perform a near-threshold visual perception task. Task performance is evaluated using Signal Detection Theory metrics. We find that the high duty cycle stimulation of the ventral anterior thalamus enhanced object recognition sensitivity. We also observe a general (i.e., region-independent) effect of LIFU on decision bias (i.e., a tendency toward a particular response) and object categorization accuracy. Specifically, high duty cycle stimulation decreases categorization accuracy, whereas low duty cycle shifts decision bias towards a more conservative stance. In conclusion, our results provide causal insight into the functional organization of the thalamus in shaping human visual experience and highlight the unique role of the transmodal-dominant ventral anterior thalamus.

INTRODUCTION

The neural basis of conscious perception remains an active area of neuroscientific investigation[1–7]. While cortical mechanisms of conscious contents have been extensively studied[8–12], the role of subcortical structures in enabling or modulating such contents remains less explored[13]. With its intricate connections to the cortex, the thalamus is a central structure that may mediate conscious experience[14–17]. Traditionally, thalamic nuclei have been categorized into specific and nonspecific types. Specific nuclei relay modal sensory information to designated cortical areas, whereas nonspecific nuclei project more broadly, regulating cortical arousal and supporting higher-order cognition[16,18,19]. For instance, the lateral geniculate nucleus (specific) relays retinal input to the primary visual cortex[20], while the intralaminar thalamus (nonspecific) are involved in controlling arousal, attention, and state of consciousness[21–23].

Recent research suggests a continuum rather than distinct categories of cortical and thalamic areas[24,25]. In the cortex, unimodal areas process sensorimotor information received from the environment, while transmodal areas further integrate this information, fostering more complex cognition[26–28]. Building on this functional organization of the cortex, our previous work revealed a unimodal-transmodal gradient in thalamocortical connectivity[29]. This thalamic functional gradient is characterized by a predominance of connectivity between the posterior thalamus and unimodal cortices, and a predominance of connectivity between the anterior/medial thalamus and transmodal cortices. This connectivity gradient also corresponds to the underlying cytoarchitecture of the thalamus, where core cells are concentrated in posterior regions and diffusely projecting matrix cells are enriched anteriorly[29,30]. Notably, research has implicated matrix cells as being crucial for conscious sensory processing[1,10,22,31–37], where a disruption of matrix-rich thalamic areas has been linked to loss of consciousness[29]. Therefore, understanding these functional and structural gradients within the thalamus is critical for elucidating the neural mechanisms underlying conscious perception.

To causally probe thalamic roles in conscious perception, precise stimulation of deep brain areas is essential. Traditional methods such as deep-brain stimulation, optogenetics, and transcranial electrical stimulation are either invasive or lack spatial resolution[38,39]. Instead, transcranial low-intensity focused ultrasound (LIFU) provides a non-invasive and precise way to target deep structures[40–46]. Although the exact mechanisms behind LIFU's effects are still being explored—with hypotheses ranging from thermal effects[47] to membrane pore formation[48] and mechanosensitive channel activation[49]—its effectiveness in modulating neural activity and behavior has been well-established[40,48,50–52]. However, its impact on conscious perception remains largely uncharted territory. Notably, the effects of LIFU are known to be influenced by parameters such as duty cycle (i.e., the percentage of time the ultrasound is actively transmitting within each pulse cycle). High duty cycles generally lead to excitation and low duty cycles to inhibition[48,49,53]. Yet, the optimal sonication parameters for modulating perception—particularly in human subcortex—are still to be determined.

In this work, we aim to elucidate the causal roles of thalamic regions in conscious perception, hypothesizing that sonicating different regions or applying different stimulation parameters (i.e., duty cycle) will lead to distinct perceptual outcomes. We specifically apply LIFU in healthy volunteers while they are performing a near-threshold visual task and evaluate changes in their visual perception using metrics derived from Signal Detection Theory (SDT). For this purpose, we sequentially stimulate four thalamic areas (ventral anterior/posterior and dorsal anterior/posterior).

Our findings reveal that the transmodal-dominant ventral anterior thalamus significantly modulates the sensitivity of conscious visual perception. Additionally, we demonstrate both common (region-independent) and duty cycle-dependent effects of LIFU on decision bias and categorization accuracy in object recognition.

RESULTS

Sixty participants (age: 25.9 ± 6.3, mean ± SD; 38 females, 22 males) were randomly assigned to one of the two duty cycle groups. One group received LIFU with a high duty cycle (70%), while the other received LIFU with a low duty cycle (5%) with equal spatial-peak temporal-average intensity of I_{spta} = 0.72 W cm^{-2} (Fig. 1a). The experiment involved several key steps, such as transducer setup, image contrast titration, and six blocks of the visual task (Fig. 1b-d). There were two outer LIFU-OFF baseline blocks (Baseline-1 and Baseline-2) and four inner LIFU-ON blocks. During each LIFU-ON block, LIFU was administered to only one of four regions of the left thalamus, including the ventral anterior (VA), ventral posterior (VP), dorsal anterior (DA), and dorsal posterior (DP) thalamus (Fig. 1e). The order of stimulated regions was pseudo-randomized and counterbalanced among participants, and each participant received a consistent duty cycle throughout the session. By including multiple targets, we could analyze in within-subject manner as a function of stimulated region.

We employed a well-established near-threshold visual object recognition and categorization task[8,9]. Stimuli were presented at the intensity close to the threshold of conscious perception. Using an adaptive staircase paradigm, we titrated the image contrast for each participant[8,54] (Fig. 1f). Four object categories were used: faces, houses, human-made objects, and animals (Fig. 1g). We also included scrambled images, which comprised 20 out of 100 trials. During each trial, participants responded to two questions: one regarding the category of the presented image (i.e., "What category did the observed image belong to?") and another concerning their subjective recognition experience (i.e., "Did you have a meaningful visual experience?") (Fig. 1h). Here, 'recognition' was operationally defined as the perception of an object that makes sense in the real world, as opposed to meaningless noise-like patterns. Therefore, the recognition rates for real and scrambled images could be interpreted as hits and false alarms, respectively (Fig. 1i).

Based on hit and false alarm rates, we evaluated sensitivity and decision bias for object recognition within the SDT framework (see Methods: Signal detection theory analysis). Sensitivity reflects the ability to differentiate between real and scrambled images, while decision bias indicates a tendency towards a particular response. Herein, a high bias signifies a tendency to say "NO" (i.e., "Didn't have a meaningful visual experience") to the recognition question (Question-2), reflecting a conservative stance in object recognition. Categorization accuracy was also quantified, independently of object recognition.

During Baseline-1, participants recognized 54.7 ± 14.7% (mean ± SD) of the real images (Supplementary Fig. 1a), which was not significantly different from the intended 50% recognition rate, confirming the successful implementation of the staircase procedure (see SI text and Supplementary Fig. 1 for statistics and additional analyses on baseline perceptual outcomes). We also found no significant differences in perceptual outcomes between the two baselines, suggesting that LIFU did not produce detectable long-lasting effects within our experimental timescale of approximately one hour (Supplementary Fig. 2).

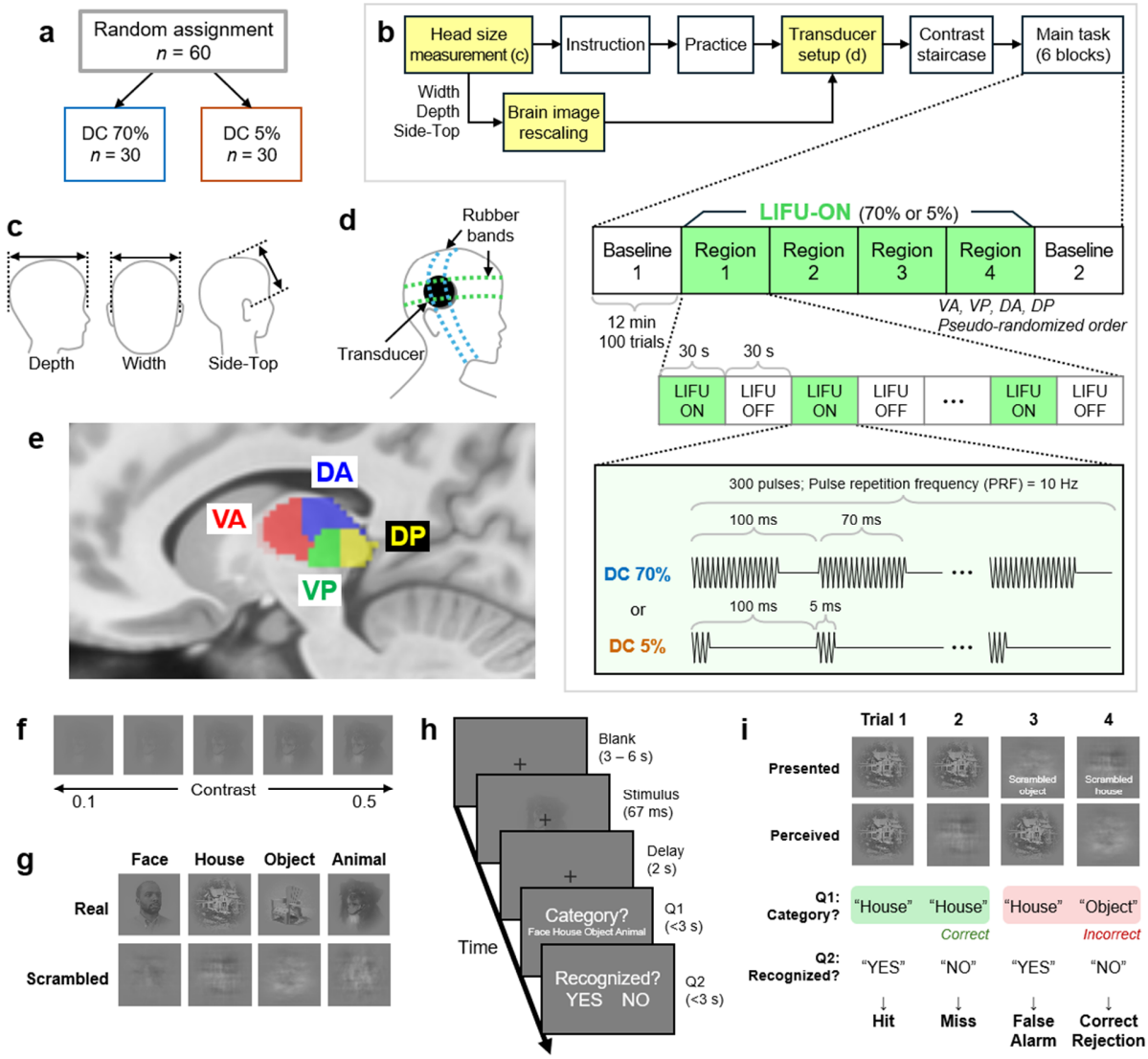

Fig. 1: Overview of the block design, experimental setup, and behavioral paradigm. a Randomized study group assignment. Sixty subjects were randomly assigned to one of two groups, each consisting of 30 participants, corresponding to either a 70% or 5% duty cycle (DC). **b** The timeline of experimental sessions, including initial preparation steps and the main task. The main task included two baseline blocks and four LIFU-ON blocks with a pseudo-randomized order of stimulation regions. Each block comprised 100 trials. Each LIFU-ON block included 12 alternating 30-second ON and OFF epochs, with each ON epoch consisting of 300 pulses of varying duty cycles (pulse repetition frequency = 10 Hz). **c** Measurement locations for head size, including width, depth, and side-to-top. **d** Illustration of the transducer fixed with two perpendicular rubber bands on the participant's head. **e** Sagittal view for the four subdivisions of the left thalamus: ventral anterior (VA), ventral posterior (VP), dorsal anterior (DA), and dorsal posterior (DP) thalamus, overlaid on standard MNI template brain images. **f** Example of an animal image displayed at different contrast levels. **g** Examples of real and scrambled images for each category (face, house, human-made object, and animal). **h** Trial structure showing the sequence of events: a blank period, stimulus presentation, delay, and two questions (categorization and recognition). **i** Illustration of the four trial types (hit, miss, false alarm, and correct rejection). Due to copyright limitations, the actual images used in our

experiment are not shown. Copyright-free images included in this figure were obtained from https://www.pexels.com.

Ultrasound beam profile and targeting accuracy

We simulated the LIFU beam *in silico* on an MNI template brain to characterize the beam profile (Fig. 2a). The beam exhibited a bullet-like shape with an aspect ratio of approximately 10, measuring 50 mm in length and 5 mm in width, in agreement with a previous study which used the identical transducer[55]. The location of peak intensity was observed at 80 mm, consistent with the device specifications. The temperature increase in the brain tissue was minimal, with a maximum recorded rise of 0.15°C (Supplementary Fig. 3).

As proof of concept, we utilized the MNI template brain image as a pseudo-anatomical reference for the stimulation procedure (see Methods for details) by rescaling the MNI template image to match each participant's head size. We independently validated the accuracy of this method by comparing the actual anatomical images and the rescaled images extracted from five individuals, confirming an average deviation of 1.7 ± 0.6 mm (Supplementary Fig. 4).

Post-hoc analysis confirmed successful targeting of each thalamic region (Fig. 2b-h). Probability density maps showed distinct targeting with minimal overlap (Fig. 2g,h). Mean lateral deviation (i.e., the distance from the target to the actual beam center, viewed from an angle perpendicular to the beam) was consistent across regions (2.3 ± 0.9 mm; Fig. 2i), validating region-level LIFU targeting. The Euclidean distance of the focal center from the target was 8.3 ± 4.1 mm, comparable to previous studies (Fig. 2j) [55]. Under the intensity setting of I_{spta} = 0.72 W cm^{-2}, the simulated intensity at the beam center was estimated to be 0.09 ± 0.07 W cm^{-2} (87.7 ± 9.0% energy loss; Fig. 2k).

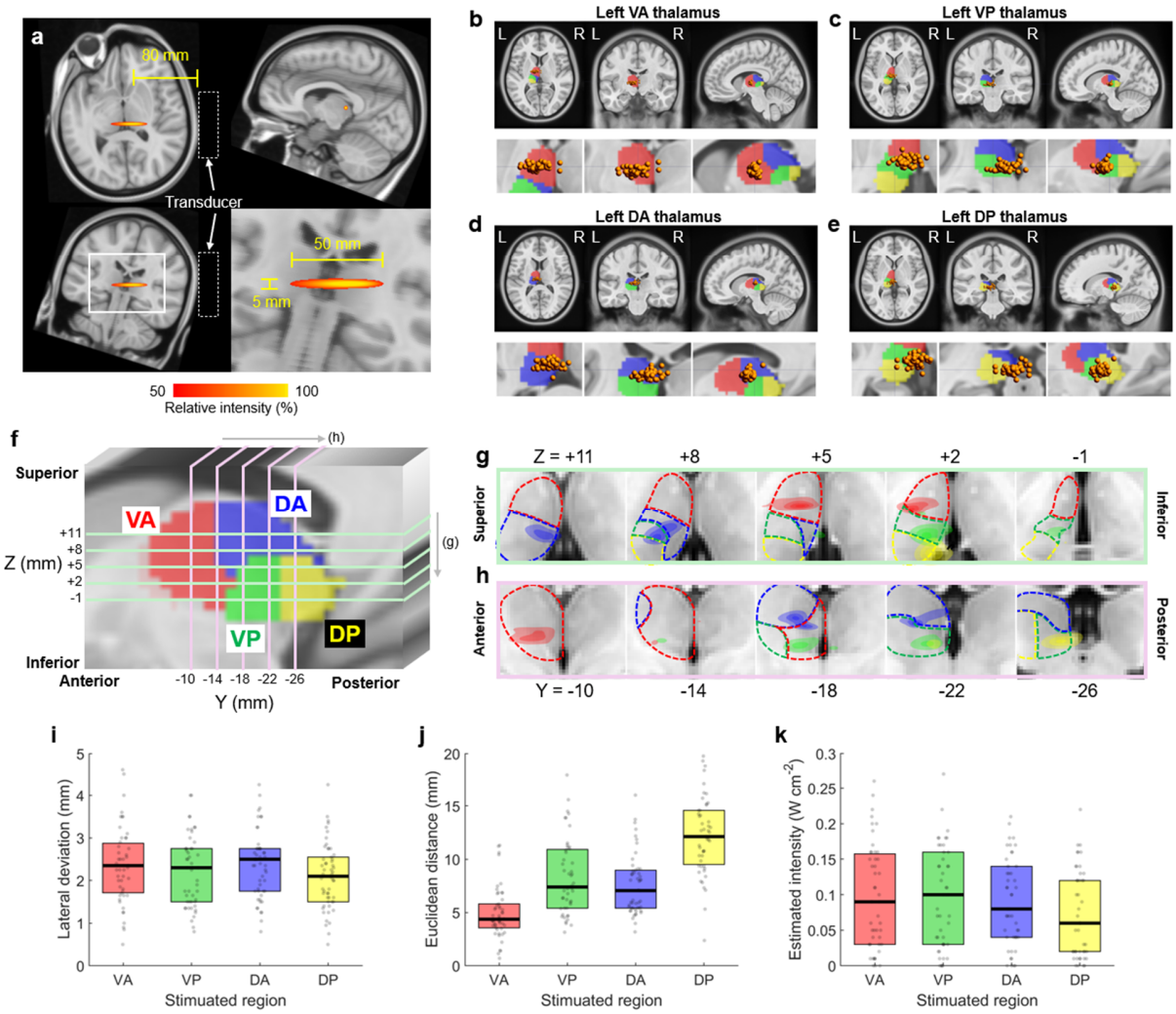

Fig. 2: LIFU beam profiles and targeting accuracy. a Geometrical profile of the LIFU beam simulated on the MNI template brain, with the transducer placed on the right temple. **b-e** Estimated beam centers in the left thalamus for each region: **b** VA, **c** VP, **d** DA, and **e** DP thalamus. VA: n = 51; VP: n = 50; DA: n = 53; DP: n = 54. Orange spheres indicate the estimated centers of the LIFU beams. The bottom images are zoomed-in views. **f** Sagittal view of the thalamus with the y and z coordinates of the cross-sections in MNI space. **g, h** Cross-sectional views displaying the probability density functions of the sonication centers for each thalamic region in the **g** x-y and **h** x-z planes. **i** Lateral deviation of beam centers from the corresponding target. VA: n = 51; VP: n = 50; DA: n = 53; DP: n = 54. **j** Euclidean distance of beam centers from the corresponding target. VA: n = 50; VP: n = 48; DA: n = 51; DP: n = 51. **k** Estimated temporal intensity at the beam centers. VA: n = 47; VP: n = 46; DA: n = 46; DP: n = 47. Box plots show the median, upper, and lower quartiles. Color coding for the thalamic regions is as follows: VA (red), VP (green), DA (blue), and DP (yellow) thalamus. VA: ventral anterior thalamus; VP: ventral posterior thalamus; DA: dorsal anterior thalamus; DP: dorsal posterior thalamus. Source data are provided as a Source Data file.

Region-specific effects of LIFU on visual perception

To mitigate individual variability, we calculated the changes of each perceptual outcome relative to the baselines (see also the results without baseline subtraction in Supplementary Fig. 5). We

performed a linear mixed-effects model ANOVA to assess both main and interaction effects specific to stimulated region and duty cycle (see Source Data for full statistics). We also conducted additional statistical tests comparing each condition against its corresponding baseline in a region-specific manner.

Sensitivity metrics (parametric: *d′* and non-parametric: *A′*) demonstrated region-specific effects, particularly for the 70% duty cycle (Fig. 3c,d). The ANOVA revealed significant main effects for both stimulated region (*d′*: $p = 0.0438$; *A′*: $p = 0.0393$) and duty cycle (*d′*: $p = 0.0463$; *A′*: $p = 0.0362$). A 70% duty cycle sonication applied to the VA thalamus resulted in a significant increase in sensitivity compared to the baseline (*d′*: $p = 0.0096$; *A′*: $p = 0.0105$). Additionally, we observed that sensitivity increase was higher when the lateral deviation of LIFU was smaller (Supplementary Fig. 6), further supporting the region-specificity of this effect.

The hit rate exhibited a significant main effect of duty cycle ($p = 0.0055$; Fig. 3a), where 70% duty cycle showed higher hit rate than 5% duty cycle. Regarding categorization accuracy, a significant decrease was observed specifically for real images under the 70% duty cycle when targeting the DA thalamus ($p = 0.0002$; Fig. 3g). No changes were detected in the false alarm rate, decision bias, or the accuracy for scrambled images ($p > 0.05$; Fig. 3b,e,f,h).

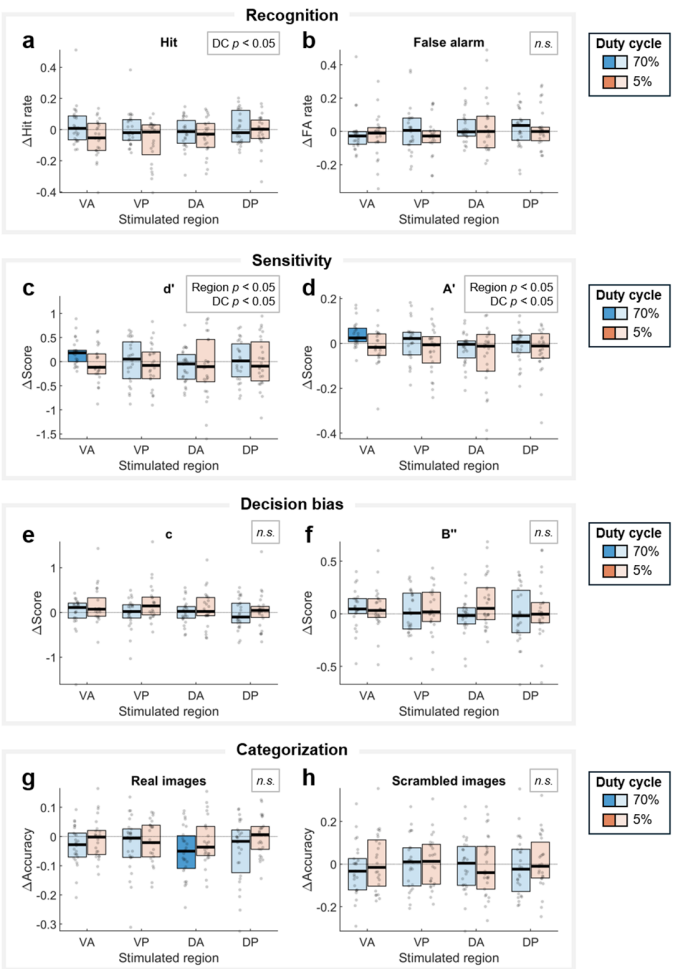

Fig. 3: Region-specific changes in recognition performance under LIFU. Changes in perceptual outcomes including **a** hit rate, **b** false alarm rate, **c** parametric sensitivity metric *d′*, **d** non-parametric sensitivity metric *A′*, **e** parametric decision bias metric *c*, **f** non-parametric decision bias metric *B″*, **g** categorization accuracy for real images**,** and **h** categorization accuracy for scrambled images. All values are baseline-subtracted. Darker solid boxes denote significant region-specific deviations from zero (FDR-corrected, $p < 0.05$, Wilcoxon signed-rank test, two-sided). ANOVA results are displayed in top-left of each subplot. The *n.s.* indicates non-significance. Box plots show the median, upper, and lower quartiles (VA 70% DC: $n = 26$; VA 5% DC: $n = 25$; VP 70% DC: $n = 26$; VP 5% DC: $n = 25$; DA 70% DC: $n = 27$; DA 5% DC: $n = 26$; DP 70% DC: $n = 27$; DP 5% DC: $n = 27$). FA: false alarm; DC: duty cycle; VA: ventral anterior thalamus; VP: ventral posterior thalamus; DA: dorsal anterior thalamus; DP: dorsal posterior thalamus. Statistics and source data are provided as a Source Data file.

Region-independent effects of LIFU on visual perception

We further investigated potential effects common to all thalamic regions, which could be masked when analyzing individual thalamic regions due to inter-subject or inter-regional variability. We thus aggregated the perceptual outcomes during the four LIFU-ON blocks (see the results without baseline subtraction in Supplementary Fig. 7; see Source Data for full statistics). We found that the hit rate exhibited a significant difference between the two duty cycles ($p = 0.0026$, Mann-Whitney U test, two-sided; Fig. 4a). Specifically, the 5% duty cycle resulted in a significant decrease in the hit rate below baseline ($p = 0.0042$, Wilcoxon signed-rank test, two-sided). Consistent with the decrease in hit rate, we observed an increase in decision bias metrics with 5% duty cycle sonication (*c*: $p = 0.0109$; *B″*: $p = 0.0510$; Wilcoxon signed-rank test, two-sided), indicating a more conservative approach in object recognition (Fig. 4e,f).

Regarding sensitivity, no significant change was observed relative to the baseline (Fig. 4c,d), although *A′* exhibited a difference between the two duty cycles ($p = 0.0224$, Mann-Whitney U test, two-sided), with a slight increase at 70% and a decrease at 5%. Categorization accuracy for real images significantly decreased under the 70% duty cycle ($p = 0.0002$, Wilcoxon signed-rank test, two-sided; Fig. 4g). No significant changes were detected for false alarm rate and accuracy for scrambled images (Fig. 4b,h).

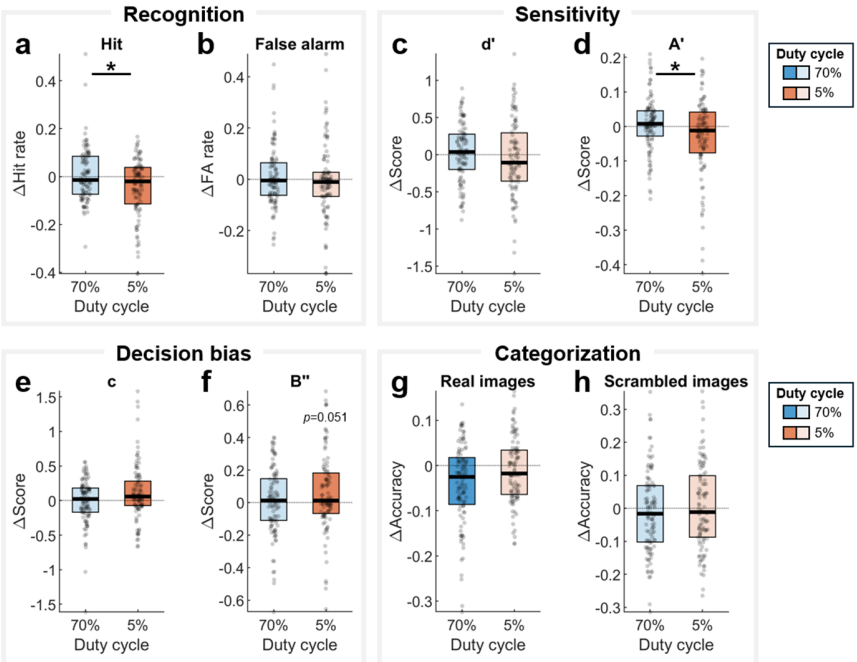

Fig. 4: Region-independent changes in visual perception under LIFU. Changes in perceptual outcomes including **a** hit rate, **b** false alarm rate, **c** parametric sensitivity metric *d′*, **d** non-parametric sensitivity metric *A′*, **e** parametric decision bias metric *c*, **f** non-parametric decision bias metric *B″*, **g** categorization accuracy for real images**, h** categorization accuracy for scrambled images. All values are baseline-subtracted. Results of four stimulated regions are aggregated. Darker solid boxes denote significant deviations from baseline zero (FDR-corrected, $p < 0.05$, Wilcoxon signed-rank test, two-sided). Asterisks indicate significant differences between two duty cycles ($p < 0.05$, Mann-Whitney U test, two-sided). Box plots show the median, upper, and lower quartiles (70% duty cycle: $n = 106$; 5% duty cycle: $n = 103$). FA: false alarm. Statistics and source data are provided as a Source Data file.

Functional connectivity of thalamic regions

To gain deeper insights into the potential large-scale neural correlates of both region-independent and region-dependent effects of LIFU on visual perception, we conducted a separate analysis to investigate the connectivity profiles of the four thalamic regions, utilizing the Human Connectome Project dataset ($n = 1009$)[56].

First, we assessed the connectivity profiles of these thalamic regions at the network level (Fig. 5a,b). In line with our prior research[29], we observed a graded shift in connectivity profiles along a unimodal-transmodal gradient. The VA thalamus displayed transmodal dominance, exhibiting higher connectivity with frontoparietal and default-mode networks compared to the other three regions (red curve in Fig. 5b). This was followed by DA thalamus, with a trend towards unimodal dominance observed in DP and VP thalamus.

Second, we examined the thalamocortical connectivity at a finer spatial scale, specifically at the voxel level. We retained the cortical voxels exhibiting the top 10% strongest connectivity with each respective thalamic region. The connectivity profiles of the four regions showed considerable overlap, particularly within the early visual cortex (cyan regions in Fig. 5c). However, region-specific connectivity patterns were also observed. The VA thalamus was predominantly

connected with the medial prefrontal cortex (mPFC) and dorsolateral prefrontal cortex (red regions in Fig. 5d). The VP thalamus exhibited unique connectivity with the somatomotor and auditory cortices (green in Fig. 5d, see also Fig. 5a). The DP thalamus showed unique clusters within various regions in the visual cortex (yellow in Fig. 5d). The connectivity profile of the DA thalamus largely overlapped with the VA thalamus (Supplementary Fig. 8), with only a few unique clusters located in regions such as left dorsolateral prefrontal cortex and right temporal-parietal junction (blue in Fig. 5d).

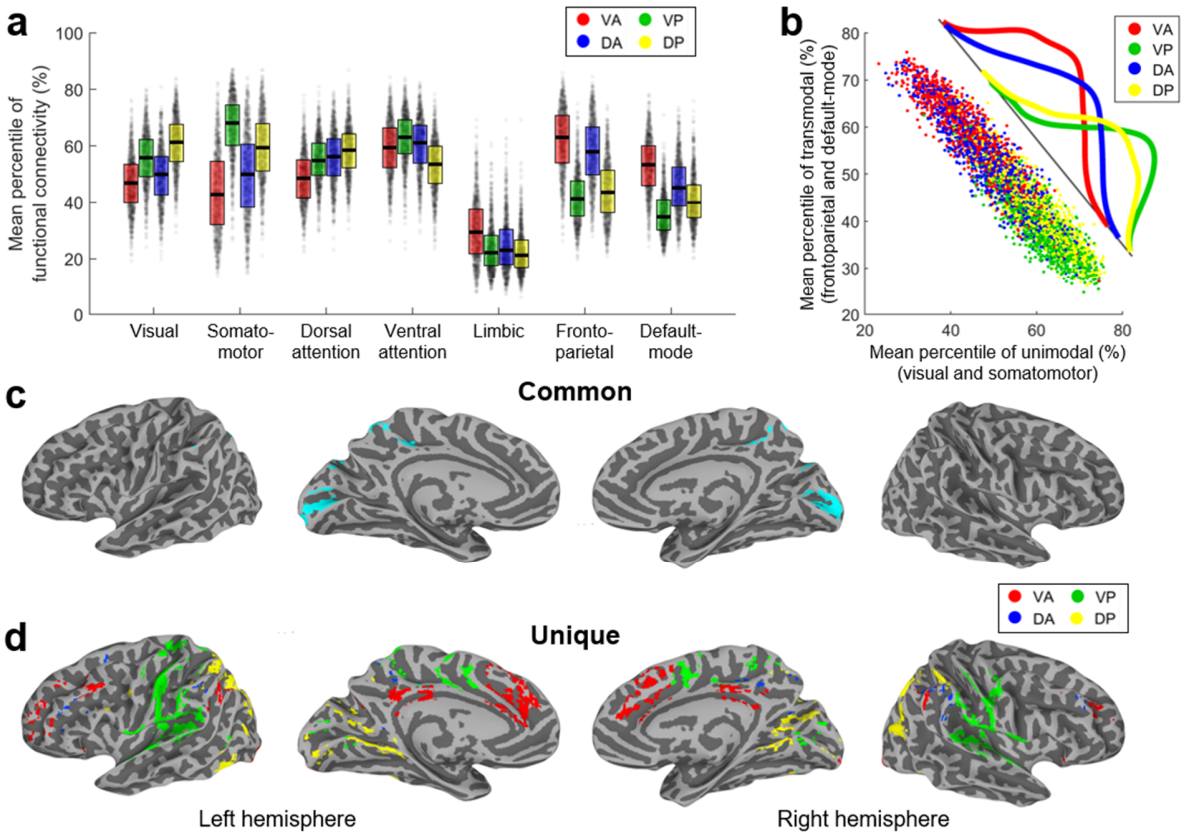

Fig. 5: Functional connectivity profiles of four thalamic regions with the cortex. a, b Network-level analysis. **a** Percentile of functional connectivity strength, averaged within each cortical network obtained from the Human Connectome Project dataset. Each dot represents an individual. Box plots show the median, upper, and lower quartiles (n = 1009). **b** Distribution of mean percentiles of functional connectivity strength for unimodal (visual and somatomotor) and transmodal (frontoparietal and default-mode) networks for each thalamic region (n = 1009). Curves represent kernel-smoothed histograms across the direction of maximal variance. **c, d** Voxel-based analysis. Cortical regions with the top 10% strongest connectivity with the thalamus, **c** common across all four thalamic regions and **d** unique to each thalamic region. VA: ventral anterior thalamus; VP: ventral posterior thalamus; DA: dorsal anterior thalamus; DP: dorsal posterior thalamus. Source data are provided as a Source Data file.

DISCUSSION

This study aimed to illuminate how different thalamic nuclei modulate conscious perception. Through targeted LIFU neuromodulation, we uncovered a unique role for the transmodal-dominant ventral anterior (VA) thalamus in modulating the sensitivity of conscious perception. Moreover, we observed both common (region-independent) and duty cycle dependent effects of LIFU on decision bias and categorization accuracy in object recognition, as summarized in Fig. 6. Notably, the VA thalamus, which played the most prominent role in conscious perception, was more closely functionally connected with medial and dorsolateral prefrontal cortex. Collectively, our research provides a valuable causal insight into the unimodal-transmodal functional organization of the thalamus.

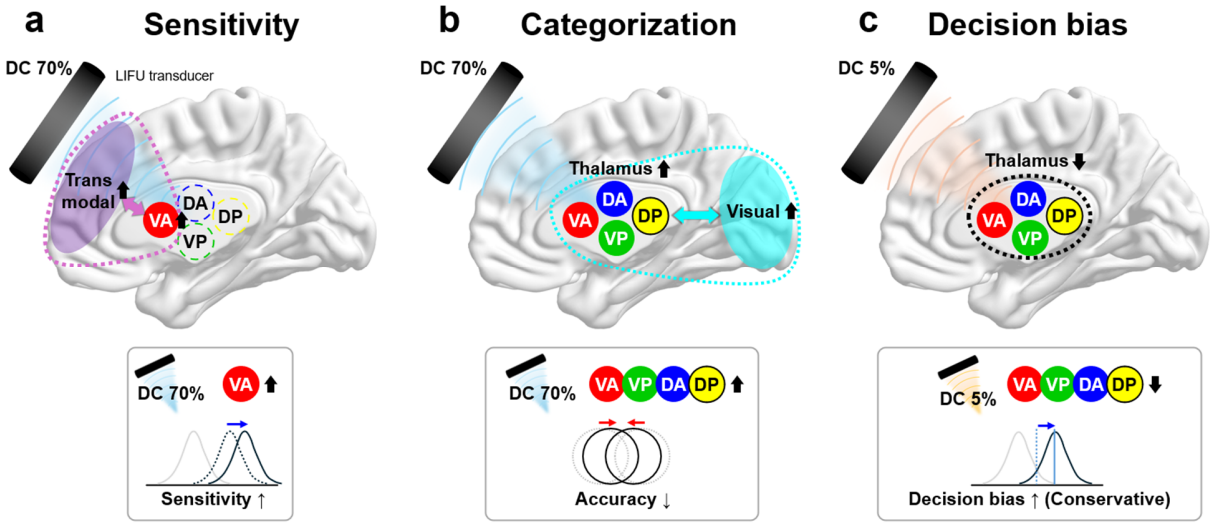

Fig. 6: Summary of LIFU effects on visual perception. a Sensitivity increases when the VA thalamus is stimulated at the 70% duty cycle. This is associated with increased functional connectivity between the VA thalamus and transmodal areas compared with other thalamic nuclei. **b** Decrease in categorization accuracy is observed nonspecifically across all thalamic regions at the 70% duty cycle, potentially driven by interactions between the thalamus and the visual network (cyan). **c** Decision bias increases (recognition being more conservative) by the 5% duty cycle in region-independent manner. VA: ventral anterior thalamus; VP: ventral posterior thalamus; DA: dorsal anterior thalamus; DP: dorsal posterior thalamus.

Our key finding is the unique role of the transmodal-dominant VA thalamus in conscious perception (Fig. 6a). Being nonspecific and matrix-rich, VA thalamus likely interacts extensively with thick-tufted layer-5 pyramidal neurons in the cortex, promoting large-scale cortical integration essential for conscious sensory processing[1,17,31,33,57]. This also support theoretical frameworks such as thalamic gating mechanisms and dendritic integration theory, suggesting that matrix cells in the higher-order thalamus may modulate the threshold for conscious perception by influencing the bursting activity of thick-tufted layer-5 pyramidal neurons in the cortex[1,17,25,58]. These matrix cells, with their diffuse connectivity, are known to facilitate the entry of sensory content into consciousness, potentially by lowering the activation threshold of layer-5 pyramidal neurons[17,36]. By activating the VA thalamus, our LIFU intervention likely increases dendritic integration in layer-

5 pyramidal neurons, promoting widespread cortical bursting, thereby increasing perceptual sensitivity (further discussion on duty cycle-dependence follows below).

Furthermore, the VA thalamus encompasses the intralaminar nuclei, with projections innervating various cortical and subcortical regions[18,23,59]. Electrical stimulation of these nuclei via implanted electrodes has been shown to awaken non-human primates from anesthesia[22,32,37] and aid in the recovery of consciousness in patients with neuropathological conditions[60–62]. Similarly, microinjection of nicotine or potassium channel-blocking antibodies into these nuclei has restored consciousness in rodents[63,64]. Moreover, previous LIFU study targeting these nuclei demonstrated improvements in patients with disorders of consciousness[65]. Our findings provide preliminary evidence that the intralaminar nuclei might influence the qualitative aspect of conscious perception, in addition to modulating the state of consciousness.

One important question is whether the increased sensitivity of conscious perception was due to the VA thalamus being excited. In contrast to prior human LIFU studies that employed only one duty cycle[55,66–68], we incorporated two duty cycles (70% vs. 5%) into our experimental design. LIFU is thought to selectively activate excitatory vs. inhibitory neurons depending on the duty cycle[48,69]. Thus, prior studies suggested that LIFU exerts a general excitatory effect at high duty cycles (e.g., > 50%) and an inhibitory effect at low duty cycles (e.g., < 20%)[49,69–72]. Based on this, we suggest that 70% duty cycle LIFU on the VA thalamus has induced an excitatory effect. This interpretation is also supported by previous studies. For example, Wu et al. demonstrated that higher pre-stimulus activity in the VA thalamus predicts greater sensitivity in conscious perception[12]. Therefore, exciting the VA thalamus may elevate its overall activity level, leading to heightened perceptual sensitivity. Furthermore, given the strong bidirectional excitatory connections[73] and functional connectivity (Fig. 5d) between the VA thalamus and transmodal areas such as the mPFC, VA thalamus stimulation with a 70% duty cycle may indirectly excite the mPFC. This is also supported by evidence that single-pulse electrical stimulation of the VA activates the mPFC[74]. Higher pre-stimulus mPFC activity also predicts greater perceptual sensitivity—a prediction intriguingly aligned with the previous findings[12]. Collectively, these observations suggest that LIFU with a 70% duty cycle induced an excitatory effect on the VA thalamus, which in turn, co-activated the mPFC. This dual activation could underlie the observed increase in perceptual sensitivity.

Regarding the region-independent decrease in categorization accuracy for real images observed with 70% duty cycle (Fig. 6b), we speculate that this effect might stem from the common functional connectivity of the thalamic regions with the visual cortex (Fig. 5c). Assuming that exciting these thalamic areas may lead to co-activation of the visual cortex, this observation aligns with previous work demonstrating a negative correlation between the pre-stimulus activity of the visual network and categorization accuracy[12].

Regarding LIFU at 5% duty cycle, we observed common (region-independent) effects that led to more conservative decision bias (Fig. 6c). We hypothesize that this duty cycle likely induced an inhibitory neural effect, aligning with a previously-reported negative correlation between pre-stimulus thalamic activity and decision bias[12]. Further supporting our interpretation, prior research showed that applying LIFU at 5% duty cycle to the thalamus produced anti-nociceptive effects, suggesting a potential inhibitory influence on sensory processing[55].

Methodologically, our work represents a significant advancement in human LIFU studies. While regional targeting within the subcortex has been previously demonstrated in rodents[49], our work

presents the first known instance of multiple regional-level stimulations within the human thalamus. We achieved targeting of each thalamic region with sub-centimeter precision, confirmed by post-hoc analysis showing minimal overlap in the distributions of the beam centers (Fig. 2g,h). Thinking of future clinical applications, we also eliminated the reliance on brain imaging in individual subjects and thus expedited the experimental procedure; our strategy used an individually rescaled template image for LIFU targeting, thereby mitigating the need for anatomical imaging, e.g., computed tomography (CT) or T1 magnetic resonance imaging (MRI). Thus, our approach could enable LIFU application in populations where MRI scans are challenging, such as in infants, individuals with implanted medical devices, or those with severe claustrophobia.

We verified that the template rescaling method that we implemented meets the desired targeting accuracy. Our strategy achieved small deviations of 1.7 ± 0.6 mm relative to the actual T1 anatomical image (Supplementary Fig. 4). The validity of the template rescaling method is also supported by effect size increase as the lateral deviation of the beam center from the intended target (as determined by rescaled template image) decreased (Supplementary Fig. 6). Notably, the average lateral deviation of the beam from the target (2.3 ± 1.0 mm, Fig. 2i) was comparable to the beam radius (2.5 mm). This was also comparable to or better than those in previous works (deviation ranging from 3 to 9 mm), reinforcing the robustness and precision of our targeting approach[55,75].

While previous research demonstrated the potential for LIFU to induce long-lasting effects ranging from hours to weeks[76–78], we did not observe persistent changes as evidenced by the comparison between Baseline-1 and Baseline-2 data (Supplementary Fig. 2). This discrepancy may be attributed to two factors. First, the estimated intensity of our LIFU stimulation (0.09 ± 0.07 W cm^{-2}) might have been insufficient to trigger long-term modifications. Second, the visual system, being highly adaptable and dynamic, might respond differently to LIFU compared to domains like addiction, anxiety, or depression where longer-term effects have been observed[72,76,77]. To better understand the implications of LIFU for scientific study and therapeutic application, future investigations should assess the factors that influence the duration of sonication effects.

Our study has limitations. First, the effect size of the LIFU-induced modulation of conscious perception was small (e.g., Cohen's $d = 0.3$ for sensitivity increase during VA thalamus excitation). This might be due to the low intensity of LIFU, primarily caused by significant energy loss (≈ 90%) from ultrasound attenuation through the human skull[79]. Further attenuation could have resulted from hair and air pockets. Advanced approaches like direct attenuation measurement and compensation may mitigate this problem[79].

Moreover, the current FDA intensity guidelines (e.g., spatial-peak temporal-average intensity I_{spta} = 0.72 W cm^{-2}) are based on diagnostic and imaging ultrasound devices, and specific guidelines for LIFU on human brain are lacking[80]. Future studies should advocate for updated FDA guidelines specific to LIFU in the human brain, as current evidence suggests that higher intensities, tested safely in animal studies, may produce more robust effects without causing thermal damage[49,81,82].

Second, the region-independent effects might be confounded by the potential influence of auditory artifacts[83]. However, the observed outcomes cannot be solely explained by auditory effects. Sonication with 5% duty cycle generated more noticeable sound due to the fixed time-averaged intensity compared to the 70% duty cycle leading to a higher percentage of participants reporting awareness of the sound at 5% (93% vs. 52% of participants, see Source Data). If auditory artifacts were the primary factor influencing the results, then we would expect the 5% duty cycle to have

398 a greater effect on perceptual outcomes, and in the same direction as the effects at the 70% duty
399 cycle. However, we observed opposite effects between the two duty cycles on measures such as
400 hit rate and sensitivity (Fig. 3a,c,d), as well as the effects unique to the 70% duty cycle such as
401 the lower categorization accuracy for real images (Fig. 4g). These findings support the specificity
402 of the observed effects. Nonetheless, to better isolate and understand the potential confounding
403 effects of auditory artifacts, future research may include a sham control with replicated sound
404 playback, or masking of the transducer sound during LIFU stimulation.

405 In conclusion, our findings illuminate the causal roles of distinct thalamic regions in conscious
406 perception, particularly highlighting the unique contribution of the transmodal-dominant ventral
407 anterior (VA) thalamus in modulating perceptual sensitivity. These results provide causal insight
408 into the intricate unimodal-transmodal functional organization of the thalamus.

409

410 **METHODS**

411 **Participants.** The study protocol (ClinicalTrials.gov ID: NCT06083493) was approved by the
412 Institutional Board Review of the University of Michigan Medical School. A total 60 participants
413 (age: 25.9 ± 6.3 years, mean ± SD; 38 females, 22 males) participated in the experiment. All
414 subjects provided written informed consent prior to the experiment and were compensated. All
415 subjects were right-handed, did not have any hearing loss, and were not colorblind, and had
416 normal or corrected-to-normal vision. Although hair shaving was not required for this study, seven
417 participants chose to shave their right temple in exchange for additional compensation.
418 Participants were assigned to one of two equal-sized groups (duty cycle = 70% and 5%) by a
419 random number generator, each comprising 30 participants. Since the neuromodulation effect is
420 dependent on various factors, such as parameters and target regions, determining a prior effect
421 size is challenging. However, we planned for a subject number of n = 30 per group, exceeding
422 the mean sample size (n = 19) reported in the literature[84]. One subject who performed a different
423 visual task was not included in data analysis. Three subjects with technical issues during targeting
424 were excluded from data analysis. One subject did not complete the task due to technical issues
425 in perceptual threshold determination. One subject was excluded because the hit rate during
426 Baseline-1 was too low (< 15%). Thus, a total sample size was n = 54 (70% duty cycle: n = 27;
427 5% duty cycle: n = 27; see also Supplementary Fig. 9 for a flow chart). Sex or gender analysis
428 was not conducted because there were no sex or gender specific hypotheses regarding the
429 influence of ultrasound neuromodulation on visual perception. Participants were blinded to the
430 intervention conditions by providing identical procedural setups and device operations across both
431 groups, ensuring that all participants did not know the specific duty cycle assignment.

432 **LIFU devices and parameters.** LIFU was administered using the BrainSonix BXPulsar 1002
433 LIFU System (BrainSonix Corporations, Sherman Oaks, CA, USA). This system includes a single
434 transducer with a 61.5 mm diameter and 80.7 mm focal depth. The focal depth was also validated
435 by Blatek Ultrasonic Transducers (Boalsburg, PA, USA). This transducer is mounted in a plastic
436 housing and sealed with a thin polyethylene membrane. To identify the optimal placement for the
437 transducer on the participant's head, we utilized the Brainsight Neuro-Navigation System (Rogue
438 Research, Montreal, Quebec, Canada).

439 Sonication parameters are determined as follows: Fundamental frequency: 650 kHz; Pulse
440 repetition frequency: 10 Hz; Pulse width: 5 ms; Duty cycle: 70% and 5%; Sonication duration: 30
441 s; Inter-sonication interval: 30 s; Sonication per block: 12; I_{spta}: 0.72 W cm^{-2}. The intensity is

calculated using the US FDA's derating method for diagnostic ultrasound systems, which assumes a uniform tissue attenuation rate of 0.3 dB cm^{-1} MHz^{-1}.

Transducer setup. Aquasonic Ultrasound Gel was applied to the right temple before positioning the transducer, ensuring that all hairs in the area were thoroughly coated with gel to enhance ultrasound transmission. The transducer was then positioned on the right temple and secured with two adjustable fabric bands: one band ran from the chin over the top of the head, and the other band passed from the forehead to the back of the head. Additional self-adhering bandages were used on top of the fabric bands to fine-tune the angle of the transducer for precise alignment. During the LIFU stimulation, we recorded the coordinates of the target location and the contact point between the transducer and the skin for post-hoc analysis.

Target locations. Following a previous thalamic parcellation scheme[85], the thalamus was coarsely divided into four regions: ventral anterior (VA), ventral posterior (VP), dorsal anterior (DA), dorsal posterior (DP). Given the lack of evidence for functional lateralization in the thalamus, we opted to target the left hemisphere for convenience. The center coordinates for the four regions in the MNI space are as follows. Left VA: (-8 mm, -11 mm, 6 mm), Left VP: (-13 mm, -23 mm, 2 mm), Left DA: (-12 mm, -23 mm, 12 mm), Left DP: (-16 mm, -31 mm, 2 mm). Notably, due to the elongated shape of the beam (Fig. 2a), it is possible that part of the right thalamus may have been partially affected.

Head size measurement. We used a digital caliper to measure head size in three dimensions: width, depth, and side-to-top distance (Fig. 1b). Head width was measured as the distance between the left and right supratragic notches, which are indentations in the ear cartilage right above the tragus. Head depth was measured from the most posterior (back) point to the most anterior (front) point of the head. The side-to-top distance was defined as the measurement from the one supratragic notch to the highest top point of the head.

Template rescaling method. We rescaled the ICBM 2009c Nonlinear Asymmetric template of the MNI152 linear template to match each participant's head size based on the three measured dimensions. The head height, defined as the height of a triangle formed by the top of the head, the supratragic notch, and the center of the head at the plane of the supratragic notch, was calculated using the formula:

$$Height = \sqrt{(Side\text{-}to\text{-}Top\ Distance)^2 - (Width)^2} \quad (1)$$

The default head size measurements of the MNI template were as follows: width: 16 cm, depth: 21 cm, and height: 15 cm. We then calculated the size ratio between the MNI template and the participant's head dimensions. The NIFTI image of the MNI template was resliced using B-spline interpolation to adjust to the participant's head size.

We performed a separate analysis with five subjects to validate the template rescaling method. For these subjects, we obtained actual anatomical T1 images and generated rescaled template images using the described method. For both the actual T1 and rescaled template images, we identified the real-space coordinates corresponding to four left thalamic regions based on their MNI-space coordinates. After coregistering the two images, we calculated the Euclidean distances between the coordinates derived from the actual T1 images and those from the rescaled template images for each thalamic region.

Ultrasound intensity and thermal simulation. We employed SimNIBS pipeline (SimNIBS v4.1.0, https://simnibs.github.io/simnibs/build/html/index.html) to differentiate skin, skull, and brain within the rescaled template brain images[86]. We then simulated the transcranial ultrasound intensity and thermal profiles using the BabelBrain software (BabelBrain v0.3.5, https://proteusmrighifu.github.io/BabelBrain/)[87]. Within the Brainsight software (v2.5.4), we created post-hoc trajectories starting from the recorded contact points between the transducer and the skin, pointing toward the thalamus. The spatial resolution of was set to points-per-wavelength = 6 and the field was simulated 100 mm beyond the target at maximum.

Experimental procedure. The experiment was conducted in a single session lasting approximately two hours (Fig. 1a). At the beginning of the session, participants' head size was measured (details above), followed by task instructions. Participants first completed a brief practice run consisting of 30 trials (a shorter version of staircase procedure; see below). Next, the ultrasound transducer was positioned, and participants underwent the main image contrast staircase procedure involving 60 trials. Participants then engaged in the main task, which consisted of six blocks, each containing 100 trials and lasting approximately 12 minutes, for a total of 600 trials (Fig. 1a). For staircase and main task, a custom-modified version of the public code implemented for the near-threshold behavioral paradigm (https://github.com/BiyuHeLab/NatCommun_Levinson2021/) was used with Psychophysics Toolbox executed on MATLAB R2024a[8,88].

During the first and last blocks, LIFU was not applied (referred to as Baseline-1 and Baseline-2). During the inner four blocks, four thalamic areas are stimulated in a pre-assigned, pseudo-randomized order (determined by a random number generator), counter-balanced across the participants, with a consistent duty cycle (either 70% or 5%) within one participant.

Visual stimuli. Visual images encompassed four categories: faces, houses, human-made objects, and animals (Fig. 1g), which were used in a previous study[8]. The images were sourced from publicly available labeled photographs or the Psychological Image Collection at Stirling (PICS). Each category included five distinct images, resulting in a total of 20 unique real images. All images were converted to grayscale and resized to 300 × 300 pixels. The pixel intensities were normalized by subtracting the mean and dividing by the standard deviation. Subsequently, the images were processed with a 2D Gaussian smoothing filter ('imgaussfilt' function in MATLAB R2024a), using a standard deviation of 1.5 pixels and a 7 × 7 pixel kernel. Scrambled images that maintain low-level features were generated for each category by randomizing the phase of the 2D Fourier transform for one image from each category.

The contrast of an image was defined as:

$$contrast = \frac{I_{max} - I_{min}}{2b} \quad (2)$$

where I_{max} and I_{min} are the intensity values of lightest and darkest pixels in the image, respectively (in the range of 0 to 255). To ensure a smooth transition to the background (set as gray, intensity = 127), the edges of all images were gradually blended by applying a Gaussian window with a standard deviation of 0.2 to the image intensity.

The stimuli were displayed on a 14-inch laptop (HP ProBook 440 G4) with a 60-Hz refresh rate LCD screen, set to the maximum screen brightness. The viewing distance between the screen and the participants' eyes was maintained at 65.8 ± 5.7 cm (mean ± SD). During the experiment, participants were asked to maintain constant eye-monitor distance. We also validated the

distance during rest periods and readjusted the position of the laptop if necessary. We did not adopt masking because masking is known to influence the visual information processing[89,90].

Image contrast staircase procedure. Before the main task, participants completed the QUEST adaptive staircase procedure[8,54] to determine the contrast value that would yield a 50% recognition rate (i.e., the rate of "YES" response to Question-2). The QUEST procedure was similar to the main task but with shorter timing parameters. The inter-trial interval was 0.75 seconds, and the delay period between the stimulus and the first question was 2 seconds. The threshold contrast was identified through a QUEST process consisting of 60 trials. Each trial was randomly assigned to one of three sets, and the staircase procedure was conducted separately for each set. Task performance was deemed acceptable if the three sets successfully converged on a specific contrast value. The staircase procedure was repeated until the convergence of the three curves was confirmed. Rather than adjusting the contrast of each image individually, the staircasing aimed for 50% recognition across all images.

Main task. Each block of the main task featured four trials per real image (80 real trials in total) and five trials per scrambled image (20 scrambled trials in total). Participants were unaware of the fact that scrambled images would appear. Participants were allowed to rest for at least 3 minutes between blocks, during which the transducer was readjusted. The entire main task took about 1.5 hours to complete.

Each trial began with a fixation cross displayed on a gray background for a randomly determined duration between 3 and 6 seconds, following an exponential distribution to prevent participants from predicting stimulus onset (Fig. 1e). The stimulus image was then shown behind the fixation cross for 8 frames (67 ms), with the image intensity linearly increasing across frames. After the stimulus disappeared, the fixation cross remained on the screen for an additional 2 seconds. Each trial concluded with two sequential questions about the stimulus, each displayed for up to 3 seconds.

Question-1 asked participants to categorize the image as a face, house, object, or animal. Participants were instructed to guess the category even if they did not consciously recognize the object (four-alternative forced-choice). Question-2 assessed their subjective experience, asking whether they had a "meaningful visual experience" of the object stimulus ("YES" or "NO"). Before the practice run, participants were told that a "meaningful" stimulus was defined as something that makes sense in the real world, as opposed to random noise or meaningless shapes. They were instructed to respond "YES" even if they recognized only part of an object. Participants provided their answers by pressing buttons on a 4-key external USB keyboard placed on their lap. If participants did not respond to Question-1, it was recorded as incorrect, and for Question-2, a lack of response was recorded as "NO."

Signal detection theory analysis. We employed signal detection theory (SDT) to examine the perceptual outcomes, focusing on sensitivity and decision bias[91–93]. Sensitivity measures the ability to distinguish between real images and scrambled images. We calculated both parametric and non-parametric sensitivity metrics through standard SDT analysis: d' and A', defined as follows:

$$d' = \Phi^{-1}(H) - \Phi^{-1}(FA) \tag{3}$$

$$A' = 0.5 + \left[\mathrm{sign}(H - FA)\frac{(H - FA)^2 + |H - FA|}{4\max(H, FA) - 4\,H \cdot FA}\right] \tag{4}$$

where Φ^{-1} is the inverse normal cumulative distribution function, H is the hit rate, and FA is the false alarm rate, respectively. High d' and A' values indicate better discrimination between real and scrambled images.

Decision bias refers to the inclination to certain response, regardless of whether the stimulus is real or scrambled. We assessed decision bias using parametric and non-parametric metrics: c and B'', defined below.

$$c = -\frac{\Phi^{-1}(H) + \Phi^{-1}(FA)}{2} \tag{5}$$

$$B'' = \mathrm{sign}(H - FA)\frac{H(1-H) - FA(1-FA)}{H(1-H) + FA(1-FA)} \tag{6}$$

High c and B'' values indicate the tendency to say "NO" to Question-2, indicating a more conservative object recognition.

Following Macmillan and Kaplan's correction, we substituted the values of false alarm or hit rate to $1 - \frac{1}{2N_{real}}$ and $\frac{1}{2N_{scram}}$ when FA = 0 or H = 1, where N_{real} and N_{scram} refers to the number of trials showing real and scrambled images, respectively[12,94].

Human Connectome Project Dataset. The dataset was obtained from the S1200 Release of the WU-Minn Human Connectome Project (HCP) database, which has been extensively described in prior studies[56]. The participants were healthy young adults aged 22 to 37 years. Participants who had completed two sessions of resting-state fMRI scans (Rest1 and Rest2) were included in our analysis, resulting in n = 1009. The data were collected using a customized Siemens 3T MR scanner (Skyra system) with multiband EPI. Each scanning session comprised two sequences with opposite phase encoding directions (left-to-right and right-to-left), each lasting 14 minutes and 33 seconds. The sequences were acquired with a repetition time (TR) of 720 ms, an echo time (TE) of 33.1 ms, and a voxel size of 2 mm isotropic. To maximize data quality and minimize bias from phase encoding direction, the sequences from each session were combined, resulting in a total of 29 minutes and 6 seconds. The denoised volumetric data, preprocessed through ICA-FIX, were accessed from the online HCP database. Further details on the resting-state fMRI data collection and preprocessing are available in previous publications[95,96]. We employed the AFNI software suite (linux_ubuntu_16_64; http://afni.nimh.nih.gov/) for further preprocessing, encompassing resampling to a 3 × 3 × 3 mm resolution, band-pass filtering within the 0.01-0.1 Hz frequency range, spatial smoothing with a 6-mm Full Width at Half Maximum isotropic Gaussian kernel, and temporal normalization to attain zero mean and unit variance.

Network-level analysis. We parcellated the cortex into 400 regions of interest (ROIs), each assigned to one of seven canonical networks: visual, somatomotor, dorsal attention, ventral attention, limbic, frontoparietal, and default-mode networks, based on a well-established parcellation scheme[97,98]. Based on the Subcortical Atlas[85], we extracted time courses of BOLD signal within the left VA, VP, DA, and DP thalamus. For each region, we calculated the functional connectivity across all 400 cortical ROIs. We then obtained the rank of the functional connectivity for each resting-state session (Rest1 and Rest2) and averaged these ranks across the seven networks and two sessions to calculate network-level connectivity. Lastly, we computed the

average rank for unimodal (visual and somatomotor) and transmodal (frontoparietal and default-mode) networks and plotted them in a 2D space.

Voxel-based analysis. Mean time courses were extracted from left VA, VP, DA, and DP thalamus, serving as seed regions for functional connectivity analysis. Seed-based maps (Pearson correlation, Fisher-*z* transformed) were generated for each participant and region. Group-level *z*-score maps were generated by standardizing individual connectivity values (subtracting the mean and dividing by the standard deviation across participants). Within the cortex, we retained the top 10% of voxels with the highest connectivity. This analysis was performed independently for Rest1 and Rest2 sessions, and their overlap was used to ensure consistency. Unique and common clusters of high-connectivity voxels were then identified for each thalamic region.

Statistics. To ensure stabilization of task performance, the first ten trials of each block were omitted from the analysis. Due to technical issues, a few participants failed to complete specific LIFU-ON blocks, which were consequently excluded from the analysis (Fig. 3, 4). The affected blocks and the number of participants were as follows: VA 70% DC (n = 1), VA 5% DC (n = 2), VP 70% DC (n = 1), VP 5% DC (n = 2), and DA 5% DC (n = 1). Additionally, for one subject in the 5% DC group, the lateral deviation value was not recorded for VP (Fig. 2i). Beam center locations were not recorded for a few participants, resulting in their omission from the beam deviation analysis (Fig. 2j). The numbers of participants with missing beam center location data were: VA (n = 4); VP (n = 6); DA (n = 3); DP (n = 3). Furthermore, the locations of the transducer on the scalp were not recorded for a few participants, leading to their exclusion from the intensity estimation analysis (Fig. 2k). The numbers of participants with missing transducer location data were: VA (n = 9); VP (n = 10); DA (n = 9); DP (n = 9).

In Fig. 3, baseline-subtracted perceptual outcomes were evaluated by two statistical tests. First, we assessed the main and interaction effects of duty cycle and stimulation region using a linear mixed-effects model ANOVA. Additionally, we tested whether the distribution of perceptual outcomes for each duty cycle and stimulation region deviated from zero using the Wilcoxon signed-rank test (two-sided). Eight tests (four regions × two duty cycles) were corrected for multiple comparisons using false discovery rate (FDR) method. In Fig. 4, baseline-subtracted perceptual outcomes were aggregated across stimulation regions and compared between the two duty cycles using the Mann-Whitney U test (two-sided). Similar to the analysis in Fig. 3, we also tested whether the distributions deviated from zero using the Wilcoxon signed-rank test (two-sided). Full statistics of main and supplementary analyses are included in Source Data.

DATA AVAILABILITY

Source data are provided with this paper. The HCP dataset is available from online repository (https://www.humanconnectome.org/).

CODE AVAILABILITY

Code for near-threshold paradigm is available at Github (https://github.com/BiyuHeLab/NatCommun_Levinson2021/)[8]. Custom-built code for template rescaling will become available at Github.

REFERENCES

1. Aru, J., Suzuki, M. & Larkum, M. E. Cellular Mechanisms of Conscious Processing. *Trends in Cognitive Sciences* **24**, 814–825 (2020).
2. Dehaene, S., Changeux, J.-P., Naccache, L., Sackur, J. & Sergent, C. Conscious, preconscious, and subliminal processing: a testable taxonomy. *Trends Cogn Sci* **10**, 204–211 (2006).
3. Dehaene, S. & Changeux, J.-P. Experimental and Theoretical Approaches to Conscious Processing. *Neuron* **70**, 200–227 (2011).
4. Koch, C., Massimini, M., Boly, M. & Tononi, G. Neural correlates of consciousness: progress and problems. *Nat Rev Neurosci* **17**, 307–321 (2016).
5. Mashour, G. A. & Hudetz, A. G. Neural Correlates of Unconsciousness in Large-Scale Brain Networks. *Trends in Neurosciences* **41**, 150–160 (2018).
6. Seth, A. K. & Bayne, T. Theories of consciousness. *Nat Rev Neurosci* **23**, 439–452 (2022).
7. Storm, J. F. *et al.* An integrative, multiscale view on neural theories of consciousness. *Neuron* S0896627324000886 (2024) doi:10.1016/j.neuron.2024.02.004.
8. Levinson, M., Podvalny, E., Baete, S. H. & He, B. J. Cortical and subcortical signatures of conscious object recognition. *Nat Commun* **12**, 2930 (2021).
9. Podvalny, E., Flounders, M. W., King, L. E., Holroyd, T. & He, B. J. A dual role of prestimulus spontaneous neural activity in visual object recognition. *Nat Commun* **10**, 3910 (2019).
10. Takahashi, N., Oertner, T. G., Hegemann, P. & Larkum, M. E. Active cortical dendrites modulate perception. *Science* **354**, 1587–1590 (2016).
11. Van Vugt, B. *et al.* The threshold for conscious report: Signal loss and response bias in visual and frontal cortex. *Science* **360**, 537–542 (2018).
12. Wu, Y., Podvalny, E., Levinson, M. & He, B. J. Network mechanisms of ongoing brain activity's influence on conscious visual perception. *Nat Commun* **15**, 5720 (2024).
13. Martín-Signes, M., Chica, A. B., Bartolomeo, P. & Thiebaut de Schotten, M. Streams of conscious visual experience. *Commun Biol* **7**, 908 (2024).

14. Bell, P. T. & Shine, J. M. Subcortical contributions to large-scale network communication. *Neuroscience & Biobehavioral Reviews* **71**, 313–322 (2016).
15. Shine, J. M. *et al.* Human cognition involves the dynamic integration of neural activity and neuromodulatory systems. *Nat Neurosci* **22**, 289–296 (2019).
16. Shine, J. M., Lewis, L. D., Garrett, D. D. & Hwang, K. The impact of the human thalamus on brain-wide information processing. *Nat Rev Neurosci* **24**, 416–430 (2023).
17. Whyte, C. J., Redinbaugh, M. J., Shine, J. M. & Saalmann, Y. B. Thalamic contributions to the state and contents of consciousness. *Neuron* **112**, 1611–1625 (2024).
18. Jones, E. G. The thalamic matrix and thalamocortical synchrony. *Trends in Neurosciences* **24**, 595–601 (2001).
19. Jones, E. G. Synchrony in the Interconnected Circuitry of the Thalamus and Cerebral Cortex. *Annals of the New York Academy of Sciences* **1157**, 10–23 (2009).
20. Usrey, W. M. & Alitto, H. J. Visual Functions of the Thalamus. *Annual Review of Vision Science* **1**, 351–371 (2015).
21. Müller, E. J. *et al.* The non-specific matrix thalamus facilitates the cortical information processing modes relevant for conscious awareness. *Cell Reports* **42**, 112844 (2023).
22. Redinbaugh, M. J. *et al.* Thalamus Modulates Consciousness via Layer-Specific Control of Cortex. *Neuron* **106**, 66-75.e12 (2020).
23. Vertes, R. P., Linley, S. B. & Rojas, A. K. P. Structural and functional organization of the midline and intralaminar nuclei of the thalamus. *Front. Behav. Neurosci.* **16**, 964644 (2022).
24. Roy, D. S., Zhang, Y., Halassa, M. M. & Feng, G. Thalamic subnetworks as units of function. *Nat Neurosci* **25**, 140–153 (2022).
25. Shine, J. M. The thalamus integrates the macrosystems of the brain to facilitate complex, adaptive brain network dynamics. *Progress in Neurobiology* **199**, 101951 (2021).
26. Huntenburg, J. M., Bazin, P.-L. & Margulies, D. S. Large-Scale Gradients in Human Cortical Organization. *Trends in Cognitive Sciences* **22**, 21–31 (2018).

27. Margulies, D. S. *et al.* Situating the default-mode network along a principal gradient of macroscale cortical organization. *Proceedings of the National Academy of Sciences* **113**, 12574–12579 (2016).
28. Murphy, C. *et al.* Distant from input: Evidence of regions within the default mode network supporting perceptually-decoupled and conceptually-guided cognition. *NeuroImage* **171**, 393–401 (2018).
29. Huang, Z., Mashour, G. A. & Hudetz, A. G. Propofol Disrupts the Functional Core-Matrix Architecture of the Thalamus in Humans. *bioRxiv* 2024.01.23.576934 (2024) doi:10.1101/2024.01.23.576934.
30. Müller, E. J. *et al.* Core and matrix thalamic sub-populations relate to spatio-temporal cortical connectivity gradients. *NeuroImage* **222**, 117224 (2020).
31. Aru, J., Suzuki, M., Rutiku, R., Larkum, M. E. & Bachmann, T. Coupling the State and Contents of Consciousness. *Front. Syst. Neurosci.* **13**, (2019).
32. Bastos, A. M. *et al.* Neural effects of propofol-induced unconsciousness and its reversal using thalamic stimulation. *eLife* **10**, e60824 (2021).
33. Honjoh, S. *et al.* Regulation of cortical activity and arousal by the matrix cells of the ventromedial thalamic nucleus. *Nat Commun* **9**, 2100 (2018).
34. Munn, B. R. *et al.* A thalamocortical substrate for integrated information via critical synchronous bursting. *Proc. Natl. Acad. Sci. U.S.A.* **120**, e2308670120 (2023).
35. Shepherd, G. M. G. & Yamawaki, N. Untangling the cortico-thalamo-cortical loop: cellular pieces of a knotty circuit puzzle. *Nat Rev Neurosci* **22**, 389–406 (2021).
36. Takahashi, N. *et al.* Active dendritic currents gate descending cortical outputs in perception. *Nat Neurosci* **23**, 1277–1285 (2020).
37. Tasserie, J. *et al.* Deep brain stimulation of the thalamus restores signatures of consciousness in a nonhuman primate model. *Sci. Adv.* **8**, eabl5547 (2022).
38. Liu, X., Qiu, F., Hou, L. & Wang, X. Review of Noninvasive or Minimally Invasive Deep Brain Stimulation. *Front. Behav. Neurosci.* **15**, (2022).

723 39. Lozano, A. M. *et al.* Deep brain stimulation: current challenges and future directions. *Nat Rev*
724 *Neurol* **15**, 148–160 (2019).
725 40. Bystritsky, A. *et al.* A review of low-intensity focused ultrasound pulsation. *Brain Stimulation* **4**,
726 125–136 (2011).
727 41. Legon, W. *et al.* Transcranial focused ultrasound modulates the activity of primary
728 somatosensory cortex in humans. *Nat Neurosci* **17**, 322–329 (2014).
729 42. Rabut, C. *et al.* Ultrasound Technologies for Imaging and Modulating Neural Activity. *Neuron*
730 **108**, 93–110 (2020).
731 43. Tufail, Y., Yoshihiro, A., Pati, S., Li, M. M. & Tyler, W. J. Ultrasonic neuromodulation by brain
732 stimulation with transcranial ultrasound. *Nat Protoc* **6**, 1453–1470 (2011).
733 44. Tyler, W. J. *et al.* Remote Excitation of Neuronal Circuits Using Low-Intensity, Low-Frequency
734 Ultrasound. *PLoS ONE* **3**, e3511 (2008).
735 45. Yoo, S.-S. *et al.* Focused ultrasound modulates region-specific brain activity. *NeuroImage* **56**,
736 1267–1275 (2011).
737 46. Tufail, Y. *et al.* Transcranial Pulsed Ultrasound Stimulates Intact Brain Circuits. *Neuron* **66**, 681–
738 694 (2010).
739 47. Darrow, D. P., O'Brien, P., Richner, T. J., Netoff, T. I. & Ebbini, E. S. Reversible neuroinhibition
740 by focused ultrasound is mediated by a thermal mechanism. *Brain Stimulation* **12**, 1439–1447
741 (2019).
742 48. Dell'Italia, J., Sanguinetti, J. L., Monti, M. M., Bystritsky, A. & Reggente, N. Current State of
743 Potential Mechanisms Supporting Low Intensity Focused Ultrasound for Neuromodulation.
744 *Front. Hum. Neurosci.* **16**, 872639 (2022).
745 49. Murphy, K. R. *et al.* Optimized ultrasound neuromodulation for non-invasive control of behavior
746 and physiology. *Neuron* (2024) doi:10.1016/j.neuron.2024.07.002.
747 50. Blackmore, J., Shrivastava, S., Sallet, J., Butler, C. R. & Cleveland, R. O. Ultrasound
748 Neuromodulation: A Review of Results, Mechanisms and Safety. *Ultrasound in Medicine &*
749 *Biology* **45**, 1509–1536 (2019).

750 51. Fomenko, A., Neudorfer, C., Dallapiazza, R. F., Kalia, S. K. & Lozano, A. M. Low-intensity
751 ultrasound neuromodulation: An overview of mechanisms and emerging human applications.
752 *Brain Stimulation* **11**, 1209–1217 (2018).
753 52. Tyler, W. J., Lani, S. W. & Hwang, G. M. Ultrasonic modulation of neural circuit activity. *Current*
754 *Opinion in Neurobiology* **50**, 222–231 (2018).
755 53. Darmani, G. *et al.* Non-invasive transcranial ultrasound stimulation for neuromodulation. *Clinical*
756 *Neurophysiology* **135**, 51–73 (2022).
757 54. Watson, A. B. & Pelli, D. G. Quest: A Bayesian adaptive psychometric method. *Perception &*
758 *Psychophysics* **33**, 113–120 (1983).
759 55. Badran, B. W. *et al.* Sonication of the anterior thalamus with MRI-Guided transcranial focused
760 ultrasound (tFUS) alters pain thresholds in healthy adults: A double-blind, sham-controlled
761 study. *Brain Stimulation* **13**, 1805–1812 (2020).
762 56. Van Essen, D. C. *et al.* The WU-Minn Human Connectome Project: An overview. *NeuroImage*
763 **80**, 62–79 (2013).
764 57. Suzuki, M. & Larkum, M. E. General Anesthesia Decouples Cortical Pyramidal Neurons. *Cell*
765 **180**, 666-676.e13 (2020).
766 58. Mukherjee, A., Lam, N. H., Wimmer, R. D. & Halassa, M. M. Thalamic circuits for independent
767 control of prefrontal signal and noise. *Nature* **600**, 100–104 (2021).
768 59. Smith, Y., Raju, D. V., Pare, J.-F. & Sidibe, M. The thalamostriatal system: a highly specific
769 network of the basal ganglia circuitry. *Trends in Neurosciences* **27**, 520–527 (2004).
770 60. Magrassi, L. *et al.* Results of a prospective study (CATS) on the effects of thalamic stimulation in
771 minimally conscious and vegetative state patients. (2016) doi:10.3171/2015.7.JNS15700.
772 61. Schiff, N. D. *et al.* Behavioural improvements with thalamic stimulation after severe traumatic
773 brain injury. *Nature* **448**, 600–603 (2007).
774 62. Schiff, N. D. *et al.* Thalamic deep brain stimulation in traumatic brain injury: a phase 1,
775 randomized feasibility study. *Nat Med* **29**, 3162–3174 (2023).

776 63. Alkire, M. T., McReynolds, J. R., Hahn, E. L. & Trivedi, A. N. Thalamic Microinjection of Nicotine
777 Reverses Sevoflurane-induced Loss of Righting Reflex in the Rat. *Anesthesiology* **107**, 264–272
778 (2007).
779 64. Alkire, M. T., Asher, C. D., Franciscus, A. M. & Hahn, E. L. Thalamic Microinfusion of Antibody to
780 a Voltage-gated Potassium Channel Restores Consciousness during Anesthesia.
781 *Anesthesiology* **110**, 766–773 (2009).
782 65. Monti, M. M., Schnakers, C., Korb, A. S., Bystritsky, A. & Vespa, P. M. Non-Invasive Ultrasonic
783 Thalamic Stimulation in Disorders of Consciousness after Severe Brain Injury: A First-in-Man
784 Report. *Brain Stimulation* **9**, 940–941 (2016).
785 66. Legon, W., Bansal, P., Tyshynsky, R., Ai, L. & Mueller, J. K. Transcranial focused ultrasound
786 neuromodulation of the human primary motor cortex. *Sci Rep* **8**, 10007 (2018).
787 67. Xia, X. *et al.* Time course of the effects of low-intensity transcranial ultrasound on the excitability
788 of ipsilateral and contralateral human primary motor cortex. *NeuroImage* **243**, 118557 (2021).
789 68. Zadeh, A. K. *et al.* The effect of transcranial ultrasound pulse repetition frequency on sustained
790 inhibition in the human primary motor cortex: A double-blind, sham-controlled study. *Brain*
791 *Stimulation* **17**, 476–484 (2024).
792 69. Yu, K., Niu, X., Krook-Magnuson, E. & He, B. Intrinsic functional neuron-type selectivity of
793 transcranial focused ultrasound neuromodulation. *Nat Commun* **12**, 2519 (2021).
794 70. Fomenko, A. *et al.* Systematic examination of low-intensity ultrasound parameters on human
795 motor cortex excitability and behavior. *eLife* **9**, e54497 (2020).
796 71. Murphy, K. R. *et al.* A tool for monitoring cell type–specific focused ultrasound neuromodulation
797 and control of chronic epilepsy. *Proceedings of the National Academy of Sciences* **119**,
798 e2206828119 (2022).
799 72. Fan, J. M. *et al.* Thalamic transcranial ultrasound stimulation in treatment resistant depression.
800 *Brain Stimulation* **17**, 1001–1004 (2024).
801 73. Yang, C. *et al.* Medial prefrontal cortex and anteromedial thalamus interaction regulates goal-
802 directed behavior and dopaminergic neuron activity. *Nat Commun* **13**, 1386 (2022).

803 74. Wu, D. *et al.* Human anterior thalamic stimulation evoked cortical potentials align with intrinsic
804 functional connectivity. *Neuroimage* **277**, 120243 (2023).
805 75. Xu, L. *et al.* Characterization of the Targeting Accuracy of a Neuronavigation-Guided
806 Transcranial FUS System In Vitro, In Vivo, and In Silico. *IEEE Transactions on Biomedical*
807 *Engineering* **70**, 1528–1538 (2023).
808 76. Mahdavi, K. D. *et al.* A pilot study of low-intensity focused ultrasound for treatment-resistant
809 generalized anxiety disorder. *Journal of Psychiatric Research* **168**, 125–132 (2023).
810 77. Mahoney, J. J. *et al.* Low-intensity focused ultrasound targeting the nucleus accumbens as a
811 potential treatment for substance use disorder: safety and feasibility clinical trial. *Front.*
812 *Psychiatry* **14**, (2023).
813 78. Yaakub, S. N. *et al.* Transcranial focused ultrasound-mediated neurochemical and functional
814 connectivity changes in deep cortical regions in humans. *Nat Commun* **14**, 5318 (2023).
815 79. Riis, T., Feldman, D., Mickey, B. & Kubanek, J. Controlled noninvasive modulation of deep brain
816 regions in humans. *Commun Eng* **3**, 1–12 (2024).
817 80. Quarato, C. M. I. *et al.* A Review on Biological Effects of Ultrasounds: Key Messages for
818 Clinicians. *Diagnostics (Basel)* **13**, 855 (2023).
819 81. Folloni, D. *et al.* Manipulation of Subcortical and Deep Cortical Activity in the Primate Brain
820 Using Transcranial Focused Ultrasound Stimulation. *Neuron* **101**, 1109-1116.e5 (2019).
821 82. Qin, P. P. *et al.* The effectiveness and safety of low-intensity transcranial ultrasound stimulation:
822 A systematic review of human and animal studies. *Neuroscience & Biobehavioral Reviews* **156**,
823 105501 (2024).
824 83. Sato, T., Shapiro, M. G. & Tsao, D. Y. Ultrasonic Neuromodulation Causes Widespread Cortical
825 Activation via an Indirect Auditory Mechanism. *Neuron* **98**, 1031-1041.e5 (2018).
826 84. Sarica, C. *et al.* Human Studies of Transcranial Ultrasound neuromodulation: A systematic
827 review of effectiveness and safety. *Brain Stimulation* **15**, 737–746 (2022).
828 85. Tian, Y., Margulies, D. S., Breakspear, M. & Zalesky, A. Topographic organization of the human
829 subcortex unveiled with functional connectivity gradients. *Nat Neurosci* **23**, 1421–1432 (2020).

86. Thielscher, A., Antunes, A. & Saturnino, G. B. Field modeling for transcranial magnetic stimulation: A useful tool to understand the physiological effects of TMS? in *2015 37th Annual International Conference of the IEEE Engineering in Medicine and Biology Society (EMBC)* 222–225 (2015). doi:10.1109/EMBC.2015.7318340.
87. Pichardo, S. BabelBrain: An Open-Source Application for Prospective Modeling of Transcranial Focused Ultrasound for Neuromodulation Applications. *IEEE Transactions on Ultrasonics, Ferroelectrics, and Frequency Control* **70**, 587–599 (2023).
88. Brainard, D. H. The Psychophysics Toolbox. *Spatial Vis* **10**, 433–436 (1997).
89. Fahrenfort, J. J., Scholte, H. S. & Lamme, V. A. F. Masking Disrupts Reentrant Processing in Human Visual Cortex. *Journal of Cognitive Neuroscience* **19**, 1488–1497 (2007).
90. Rolls, E. T., Tovée, M. J. & Panzeri, S. The Neurophysiology of Backward Visual Masking: Information Analysis. *Journal of Cognitive Neuroscience* **11**, 300–311 (1999).
91. Stanislaw, H. & Todorov, N. Calculation of signal detection theory measures. *Behavior Research Methods, Instruments, & Computers* **31**, 137–149 (1999).
92. Tuzlukov, V. P. *Signal Detection Theory*. (Birkhäuser Boston, Boston, MA, 2001). doi:10.1007/978-1-4612-0187-8.
93. Wickens, T. D. *Elementary Signal Detection Theory*. (Oxford Univ. Press, Oxford, 2002).
94. Macmillan, N. A. & Kaplan, H. L. Detection theory analysis of group data: Estimating sensitivity from average hit and false-alarm rates. *Psychological Bulletin* **98**, 185–199 (1985).
95. Smith, S. M. *et al.* Resting-state fMRI in the Human Connectome Project. *NeuroImage* **80**, 144–168 (2013).
96. Glasser, M. F. *et al.* The minimal preprocessing pipelines for the Human Connectome Project. *NeuroImage* **80**, 105–124 (2013).
97. Schaefer, A. *et al.* Local-Global Parcellation of the Human Cerebral Cortex from Intrinsic Functional Connectivity MRI. *Cerebral Cortex* **28**, 3095–3114 (2018).
98. Thomas Yeo, B. T. *et al.* The organization of the human cerebral cortex estimated by intrinsic functional connectivity. *Journal of Neurophysiology* **106**, 1125–1165 (2011).

ACKNOWLEDGEMENTS

We express our sincere gratitude to our study coordinators, Amy McKinney and Aaron Ellis, for their invaluable contributions to participant recruitment, meticulous scheduling, and ensuring the smooth execution of this study. This work was supported by the National Institute of General Medical Sciences of the National Institutes of Health grants R01GM103894 (to A.G.H. and Z.H.). The content is solely the responsibility of the author and does not necessarily represent the official views of the National Institutes of Health.

AUTHOR CONTRIBUTIONS STATEMENT

H.J. and Z.H. designed the study and set up the experimental apparatus. H.J. devised the template rescaling method and developed the code. H.J., P.F., and Z.H. conducted the experiments. H.J. analyzed the data, prepared the figures, and drafted the manuscript. Z.H. co-analyzed the data. Z.H., G.A.M. and A.G.H. interpreted the data and edited the manuscript.

COMPETING INTERESTS STATEMENT

The authors declare no competing interests.